Supplemental Information: Deconfinement of Mott Localized Electrons into Topological and Spin-Orbit Coupled Dirac Fermions

José M. Pizarro,[1, 2, *] Severino Adler,[3, 4] Karim Zantout,[5] Thomas Mertz,[5]
Paolo Barone,[6] Roser Valentí,[5] Giorgio Sangiovanni,[3] and Tim O. Wehling[1, 2, †]

[1]*Institute for Theoretical Physics, University of Bremen, Otto-Hahn-Allee 1, 28359 Bremen, Germany*
[2]*Bremen Center for Computational Material Sciences,*
University of Bremen, Am Fallturm 1a, 28359 Bremen, Germany
[3]*Institut für Theoretische Physik und Astrophysik and Würzburg-Dresden Cluster of Excellence ct.qmat,*
Universität Würzburg, 97074 Würzburg, Germany
[4]*Institute of Solid State Physics, TU Wien, A-1040 Vienna, Austria*
[5]*Institute of Theoretical Physics, Goethe University Frankfurt am Main, D-60438 Frankfurt am Main, Germany*
[6]*Consiglio Nazionale delle Ricerche, Institute for Superconducting and Innovative Materials and devices (CNR-SPIN),*
c/o University "G. D'Annunzio" , Chieti 66100, Italy

SUPPLEMENTARY DISCUSSION

A.   Stacking potential energy landscapes

Here we study the dependence of the total energies of 1T-TaSe$_2$ bilayers on the local atomic stacking (Supplementary Figure 1a) and the stacking of the CCDW centers (Supplementary Figure 1b).

Dependencies on the local atomic stacking can be inferred from the stacking potential energy landscapes derived from our DFT calculations for undistorted bilayers of 1T-TaSe$_2$. The non-twisted and 180° twisted cases are shown in Supplementary Figure 1a. For non-twisted bilayer, Ta from the top layer above Ta from the bottom layer (stacking I) is the most stable configuration. Top layer Ta above bottom layer Se (stacking III) results to be a local minimum. For 180° twisted bilayer, the most stable configurations are given for Ta on top of Se (stackings III and V). Regarding the local atomic arrangement, the honeycomb stacking discussed in the main text corresponds to configuration III.

Energy differences between different stacking configurations of the CCDW centers in the distorted non-twisted 1T-TaSe$_2$ bilayers are given in Supplementary Figure 1b with the labeling of the configurations being defined in Supplementary Figure 1c: AA, AB and AC refers to CCDW centers of the top layer on top of a Ta atom from the bottom layer (local configuration I). Both, AtX and AbX refer to arrangements, where the Ta atom in the CCDW centers from one layer is on top of / beneath Se atom sites in the other layer (local configurations III and V, respectively). In this notation, At3 is the honeycomb stacking that is considered in the main text.

It becomes clear that the undistorted bilayer (Supplementary Figure 1a) already gives a good overall estimate of the total stacking differences energies of the CCDW bilayer (Supplementary Figure 1b). Hence, also in the CCDW case, the stacking potential energy landscape is dominated by contributions from the local atomic stacking.

In the CCDW non-twisted bilayer, the total stacking energies using DFT-D2 and DFT-D3 calculations are similar, with a small deviation for the most unfavorable stackings AbX (local configuration V). The resulting crystal and band structures in both methods (not shown) are also equivalent. The energy differences between Ta on top of Ta (AA, AB, AC) and Ta on top of Se above the Ta plane (At1, At2, At3) are relatively small, i.e. on the order of 10 meV per f.u.. This means that the potential energy landscapes are very flat, which is in line with realizations of multiple stacking configurations in experiments.

Assuming that the 180° twisted bilayer is similar to non-twisted case in that the potential energy landscape is dominated by contributions from the local atomic stacking, we expect that stackings AtX and AbX are the most stable ones in the 180° twisted case. This would support formation of the honeycomb pattern in the 180° twisted case, while again flat potential energy landscapes are expected.
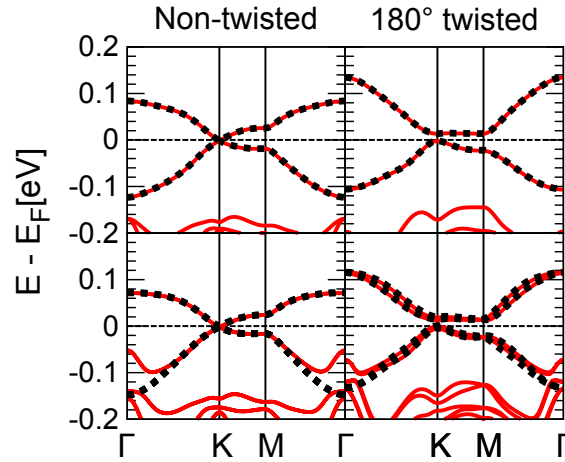
B.   Wannier tight-binding model

The relevant subspace $\mathcal{B}$ for the low-energy bands of (distorted) CCDW 1T-TaSe$_2$ monolayer and bilayer contains mainly d_{z^2} orbitals from Ta atoms in the centers of the stars-of-David (SoD, see Fig. 1). We construct a corresponding
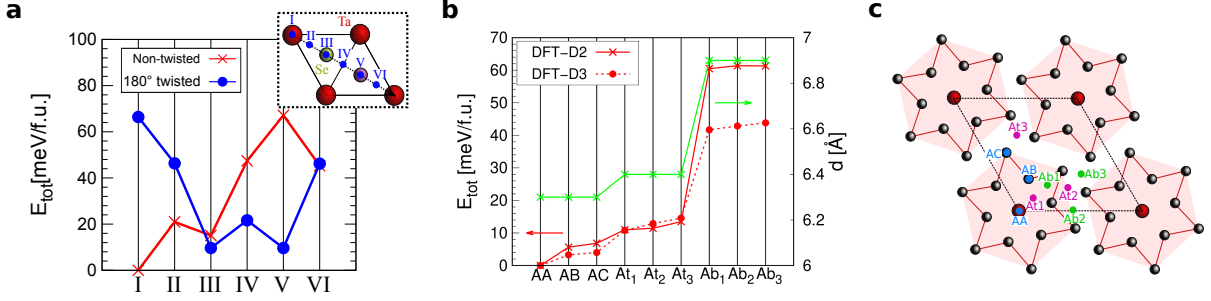
Supplementary Figure 1. **Stacking potential landscapes for 1T-TaSe₂ bilayers. a,** Potential energies for undistorted 1T-TaSe₂ bilayer in the non-twisted and 180° twisted cases. The inset shows the nomenclature of the different stacking configurations I-VI with bottom layer Ta atoms in red and Se atoms above and below the bottom Ta plane in green and pink, respectively. The stacking of the top layer is marked with blue dots and latin numbers. Blue dots refer to the position of the Ta atom in the top layer, starting from the perfectly aligned bilayer in I. Non-twisted bilayer shows a total minimum for stacking I (perfect alignement), and a local metastable minimum for stacking III (Ta on top of the Se above the Ta plane). For 180° twisted bilayer, stackings III and V are degenerate and are the most stable configurations. In the ideal honeycomb stacking, the CCDW 1T-TaSe₂ bilayers have a local stacking with the Ta in the top layer (approximately) above Se in the bottom layer, i.e. configurations III and V. **b,** Total energies per formula unit and interlayer distances d versus stacking configurations in the CCDW non-twisted bilayer 1T-TaSe₂ as obtained within the DFT-D2 and DFT-D3 approaches. **c,** Nomenclature used for the different CCDW stackings, where blue, green and magenta dots describe the location of the Star-of-David (SoD) centers from the top layer. Thus, stacking AA corresponds to perfectly aligned CCDW bilayer. Stackings AtX stand for SoD central Ta atom from the top layer aligned to the Se atom above the Ta plane from the bottom layer, and AbX for SoD center from the top layer above the Se atom below the Ta plane from the bottom layer. DFT-D2 and DFT-D3 calculated energies are similar, with a discrepancy of approximately 20 meV per f.u. for the AbX stackings. For Ta on top of Ta (AA, AB, AC) and Ta on top of Se above the lower Ta plane (At1, At2, At3) energy differences are ≲10 meV per f.u.. Stacking At3 is the one considered in the main text.

Supplementary Figure 2. *Ab-initio* **DFT band structure versus Wannierization for non-twisted and 180° twisted CCDW 1T-TaSe₂ bilayer**. DFT bands (red solid lines) are compared with our Wannier tight-binding model (black dashed lines) for non-twisted (left panels) and 180° twisted (right panels) bilayers. Top panels show the case without SOC included, the bottom panels with SOC taken into account. Our Wannier tight-binding models fit the DFT band structures obtained for CCDW 1T-TaSe₂ bilayers very well.

minimal tight-binding model using WANNIER90 code [1]. The Wannier basis is $\mathcal{B} = \{d_{z^2}^{top}, d_{z^2}^{bottom}\}$ for each spin, where the superscripts refer to SoD center Ta atom from top and bottom layers. We use a Γ-centered **k**-mesh of 9×9×1 if SOC is not included in the calculation, and Γ-centered **k**-mesh of 6×6×1 when SOC is included. In the latter case, an inner energy window covering states at K (and K') and M is considered, while leaving out the ones at Γ. We show in Supplementary Figure 2 the comparison between the DFT bands and our Wannier tight-binding model. Our model captures very well the low-energy bands of non-twisted and twisted CCDW 1T-TaSe₂ bilayers.

C. $k \cdot p$ model of low energy bands

We derive the effective model describing the low-energy band structure around the K and K' points by using the $\mathbf{k} \cdot \mathbf{p}$ perturbation theory [2, 3] for the perturbed Hamiltonian $H = H_\mathrm{I} + H_\mathrm{II} + H_\mathrm{III}$, including Pauli-type spin-orbit interaction, where:

$$H_\mathrm{I} = \frac{\hbar}{m} \mathbf{k} \cdot \mathbf{p} \tag{1}$$

$$H_\mathrm{II} = \frac{\hbar}{4m^2c^2}(\nabla U \times \mathbf{p}) \cdot \boldsymbol{\sigma} \equiv \frac{\hbar}{4m^2c^2}\mathbf{A} \cdot \boldsymbol{\sigma} \tag{2}$$

$$H_\mathrm{III} = \frac{\hbar^2}{4m^2c^2}(\nabla U \times \mathbf{k}) \cdot \boldsymbol{\sigma} \equiv \frac{\hbar^2}{4m^2c^2}(\mathbf{k} \times \boldsymbol{\sigma}) \cdot \nabla U. \tag{3}$$

The non-zero matrix elements of such perturbed Hamiltonian can be determined from group theory and exploiting the transformation properties of the one-electron wave functions under the symmetry operations of the high-symmetry point K. The knowledge of the little group of K allows to define a set of linear equations [4]:

$$\langle u^\mu_\nu | O^\alpha_\beta | u^i_j \rangle = \frac{1}{h} \sum_R \sum_{\nu'\beta'j'} {}^\mu D^*_{\nu'\nu}(R) {}^\alpha D_{\beta'\beta}(R)$$
$$\times {}^i D_{j'j}(R) \langle u^\mu_{\nu'} | O^\alpha_{\beta'} | u^i_{j'} \rangle \tag{4}$$

where h is the order of the group, u^μ_ν represents the ν-th component of the basis function of a representation μ and O^α_β is an operator that transforms like the β-th component of the basis function of a representation α, while ${}^i D_{j'j}(R)$ is the $(j'j)$ element in the matrix representative of the group element R in the i-th representation. The non-twisted (180°-twisted) CCDW bilayer belongs to the $P\bar{3}$ ($P3$) space group; both structures display a three-fold rotation C_3 around an axis perpendicular to the bilayer, while the non-twisted stacked bilayer is also centrosymmetric, the two layers being inversion partners. At point K only C_3 symmetry is preserved, and non-relativistic bands can be grouped in a one-dimensional single-valued irreducible representation (IR) K_1 and in two-fold degenerate K_2K_3 IR for the space group $P\bar{3}$; when the symmetry is lowered to $P3$, bands belonging to K_2 and K_3 are not degenerate anymore. The single-valued IRs, the corresponding characters and the basis functions are listed in Table 1. By introducing a general operator $\boldsymbol{\pi}$ with components

$$\pi_1 = p_z, \quad \pi_2 = \frac{1}{\sqrt{2}}(p_x + i\,p_y), \quad \pi_3 = \frac{1}{\sqrt{2}}(p_x - i\,p_y), \tag{5}$$

each trasforming as K_1, K_2 and K_3, respectively, one can use equation (4) to identify its symmetry-allowed non-zero expectation values on the basis functions ϕ_2, ϕ_3 spanning the K_2K_3 IR:

$$\langle \phi_2 | \pi_3 | \phi_3 \rangle, \quad \langle \phi_3 | \pi_2 | \phi_2 \rangle, \quad \langle \phi_2 | \pi_1 | \phi_2 \rangle, \quad \langle \phi_3 | \pi_1 | \phi_3 \rangle. \tag{6}$$

In this basis, therefore, the following $\mathbf{k} \cdot \mathbf{p}$ model is found to fulfill the point-group symmetries of the wave vector at K:

$$H = \begin{pmatrix} \lambda_1\sigma_z + \alpha_1(k_x\sigma_y - k_y\sigma_x) & -\hbar v_f k_+ + \lambda_R(i\sigma_x - \sigma_y) + \lambda_D k_+\sigma_z \\ -\hbar v_f k_- - \lambda_R(i\sigma_x + \sigma_y) + \lambda_D k_-\sigma_z & \lambda_2\sigma_z + \alpha_2(k_x\sigma_y - k_y\sigma_x) \end{pmatrix} \tag{7}$$

where $k_\pm = k_x \pm ik_y$ and we introduced the following parametrization:

$$v_f = \frac{1}{2m}\langle \phi_2 | p_x - ip_y | \phi_3 \rangle$$

$$\lambda_1 = \frac{\hbar}{4m^2c^2}\langle \phi_2 | A_z | \phi_2 \rangle$$

$$\lambda_2 = \frac{\hbar}{4m^2c^2}\langle \phi_3 | A_z | \phi_3 \rangle$$

$$\lambda_R = -i\frac{\hbar}{4m^2c^2}\frac{1}{2}\langle \phi_2 | A_x - iA_y | \phi_3 \rangle$$

$$\lambda_D = -i\frac{\hbar^2}{4m^2c^2}\frac{1}{2}\langle \phi_2 | (\nabla U)_x - i(\nabla U)_y | \phi_3 \rangle$$

$$\alpha_1 = \frac{\hbar^2}{4m^2c^2}\langle \phi_2 | (\nabla U)_z | \phi_2 \rangle$$

$$\alpha_2 = \frac{\hbar^2}{4m^2c^2}\langle \phi_3 | (\nabla U)_z | \phi_3 \rangle. \tag{8}$$

The effective model must also obey time-reversal symmetry $\Theta = \hat{T}K$, where K is the complex conjugation and $\hat{T} = i\sigma_y\mathbb{1}$. However, since K point is not time-reversal invariant, acting with the Θ operation will map the Hamiltonian relative to point K to the time-reversal partner K'. Additionally, inversion symmetry also must be enforced for the non-twisted honeycomb structure, where the inversion operation $\hat{P} = \mathbb{1}S_x$, swapping the basis functions, also maps the Hamiltonian equation (7) from point K to point K'. Here $\mathbf{S}$ represents the sublattice pseudospin, spanning the two-dimensional space defined by the basis functions ϕ_2, ϕ_3.

Imposing both time-reversal and inversion invariance, one finds that $\lambda_R = 0$, $\lambda_D = 0$ and:

$$\lambda_1 = -\lambda_2 \equiv -\lambda_{\text{SOC}} \qquad \alpha_1 = -\alpha_2 \equiv \alpha_{R2} \tag{9}$$

recovering the effective $\mathbf{k}\cdot\mathbf{p}$ model of equation (1) in the main text, describing the low-energy band structure around K, K' points of non-twisted honeycomb CCDW bilayer. Imposing only time-reversal symmetry, as relevant for the twisted CCDW bilayer, implies that all terms appearing in equation (7) are allowed by symmetry. Furthermore, the lack of inversion symmetry (coinciding here with a sublattice-symmetry breaking) removes all degeneracies of the unperturbed non-relativistic bands, thus introducing an effective mass term M that acts as a staggered potential. By introducing the following parametrization:

$$B = \frac{1}{2}\left(\lambda_1 + \lambda_2\right) \qquad \lambda_{SOC} = \frac{1}{2}\left(\lambda_1 - \lambda_2\right)$$
$$\alpha_{R1} = \frac{1}{2}\left(\alpha_1 + \alpha_2\right) \qquad \alpha_{R2} = \frac{1}{2}\left(\alpha_1 - \alpha_2\right) \tag{10}$$

we recover the low-energy model equation (2) in the main text, describing the band structure in the vicinity of the K, K' points.

We conclude this appendix noticing that the low-energy Hamiltonian equation (7) almost coincides with the one derived in Ref. [5] for a graphene-based system with C_{3v} symmetry, but for the additional spin-momentum coupling term parametrized by λ_D and allowed here by the lower C_3 symmetry. In fact, a minimal tight-binding model reproducing the low-energy band structure in the vicinity of K and K' points can be derived following the general scheme outlined in Ref. [5] and taking into account the reduced symmetry. Alongside the intrinsic SOC (next-nearest neighbor spin-conserving hopping, that is sublattice dependent due to lack of sublattice symmetry, parametrized here by λ_1, λ_2), the lack of any horizontal reflection allows for the so-called "pseudospin inversion asymmetric" SOC [6] (next-nearest neighbor spin-flipping hopping, also sublattice dependent, parametrized here by α_1, α_2) and, together with inversion-symmetry breaking, for the Rashba SOC [7] (nearest-neighbor spin-flipping hopping, parametrized by λ_R). The *no-go* arguments of Ref. [5] also implies that the lack of any vertical reflections in the C_3 structural symmetry allows for a purely imaginary nearest-neighbor spin-conserving SOC hopping, whose coupling constant can be parametrized by λ_D.

We obtain all effective parameters entering in the low-energy models around K and K' from a first-order Taylor expansion in k-space of the Wannier tight-binding models described above in terms of the external field E_z, see Supplementary Figure 3.

|	E	3^+	3^-	basis functions
K_1	1	1	1	P_z, A_z
K_2	1	ω	ω^*	$P_x + iP_y$, $A_x + iA_y$
K_3	1	ω^*	ω	$P_x - iP_y$, $A_x - iA_y$

Supplementary Table 1. Character table for the little group at K. Here $\omega = e^{i\frac{2\pi}{3}}$, and $\boldsymbol{P}(\boldsymbol{A})$ stands for polar (axial) vector. Notice that polar and axial vectors transform in the same way under the symmetry operations of C_3 point group.

D. Topology

The topological properties of the twisted and non-twisted TaSe$_2$ bilayers without the effects of correlation are studied using the Wannier charge center evolution, as described in [8]. Using the Wannier tight-binding Hamiltonians as input, we determine the Z$_2$ invariant to assess whether they describe a trivial or a quantum spin Hall insulator.

For the non-twisted structure we find that the Z$_2$ invariant equals 1 for all values of the electric field between 0 and 0.43 mV Å^{-1} while Z$_2$=0 for all other E-field strengths. For the 180° twisted bilayer we find Z$_2$=0 for all calculated E-field strengths instead.

In order to understand why the 180° twisted bilayer does not show any topologically non trivial phases we analyze the influence of the terms entering the Hamiltonian $H_{180°}$ from equation (2) of the main text. We proceed from the
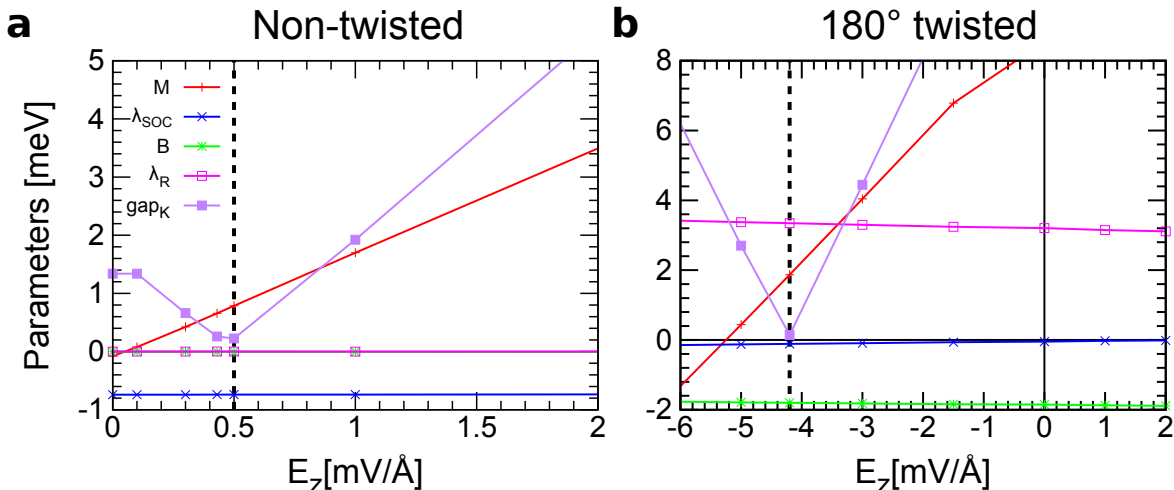
Supplementary Figure 3. **Parameters of the $k \cdot p$ expansion around Brillouin zone corners K, K' of the Wannier Hamiltonitans**. Parameters for **a,** non-twisted and **b,** 180° twisted CCDW 1T-TaSe$_2$ bilayer in vertical electric fields. The Semenoff mass M, Kane-Mele SOC λ_{SOC}, spin-valley coupling B, and Rashba SOC λ_{R} are shown as function of vertical electric field E_{z}.

Wannier Hamiltonian of the non-twisted bilayer and artificially add and vary parameters occurring in $H_{180°}$ from equation (2). Specifically, we consider a parameter space, where we vary the Semenoff mass M, the Rashba-spin orbit term λ_{R} and the spin-valley coupling term / valley Zeeman B. To determine the topological properties of non-interacting Hamiltonians in this parameter space, it turns out to be numerically efficient to track the minimal gap in the band structure and to identify connected regions of the parameter space with strictly non-zero gap, which are bounded by a submanifold of the parameter space with zero gap. If one point inside has $Z_2 \neq 0$ ($Z_2 = 0$) the whole region is topologically non-trivial (trivial). The resulting topological phase diagrams are shown in Fig. 3c of the main text.

It is useful to compare our system to the well-known case of the ideal Kane-Mele model [7]. The characteristic shape of the phase-diagram with the Rashba coupling (λ_{R}) on the y-axis and the staggered potential M (referred to as Semenoff mass) on the x-axis in the ideal Kane-Mele model resembles that of an onion [7]. We observe this behavior for the non-twisted case, see leftmost panel of Fig. 3c. The yellow horizontal line represents the trajectory of our Hamiltonian upon changing the electric field E_{z}. The main effect of E_{z} is to change M according to $M \approx M_0 + eE_{\mathrm{z}}d/\epsilon_\perp$ (see Supplementary Figure 3) and hence E_{z} drives the 0∘ twisted system from inside the topological region to the outside.

Upon twisting, we reduce the symmetry from D_{6h} to C_{3v} consequently switching on various terms in $H_{180°}$, as described in Ref. [5], among which the most important ones are the previously-mentioned Semenoff mass M, Rashba-spin orbit λ_{R} and the spin-valley coupling B. The main effect of B is to shift two of the bands having the same sublattice but different spin character at the K-point towards each other. This yields a deformed onion as topological region, where the topological region on the λ_{R} axis is reduced. (See Fig. 3c of the main text for the case of $B/\lambda_{\mathrm{SOC}} = 0.9$.) Eventually when $|B| = |\lambda_{\mathrm{SOC}}|$ the topological non-trivial region is completely suppressed and only a vertical band touching line remains, which, however, does not separate a trivial from a non-trivial region. The latter case is similar to the phase diagram of the 180° twisted TaSe$_2$ bilayer. The effects of B and λ_{R} can, thus, qualitatively explain the differences observed for the topological phases of the non-twisted and 180° twisted structure. In the 180° twisted structure, λ_{SOC} is additionally strongly reduced, which further contributes to suppressing the QSH phase. Following this line of argumention the electric field in the 180° twisted case induces a gap closing and a reopening but does not induce a topological phase transition.

In the non-twisted case, where we find QSH states in absence of interactions, we study the impact of correlations on the topological phase diagram within the TPSC approach. These calculations confirm the generic shape of the schematic phase diagram shown in (Fig. 2e).

It is known [9] that sufficiently strong Coulomb repulsion U can change the nature of the topological phase transition between QSH and band insulator from continuous with a band-touching point at the transition – as in the non-interacting Kane-Mele or Bernevig-Hughes-Zhang models – to first-order with discontinuous jump of the gap (solid line in Fig. 2e). Since the electric field E_{z} directly controls M, one can possibly tune the non-twisted system through
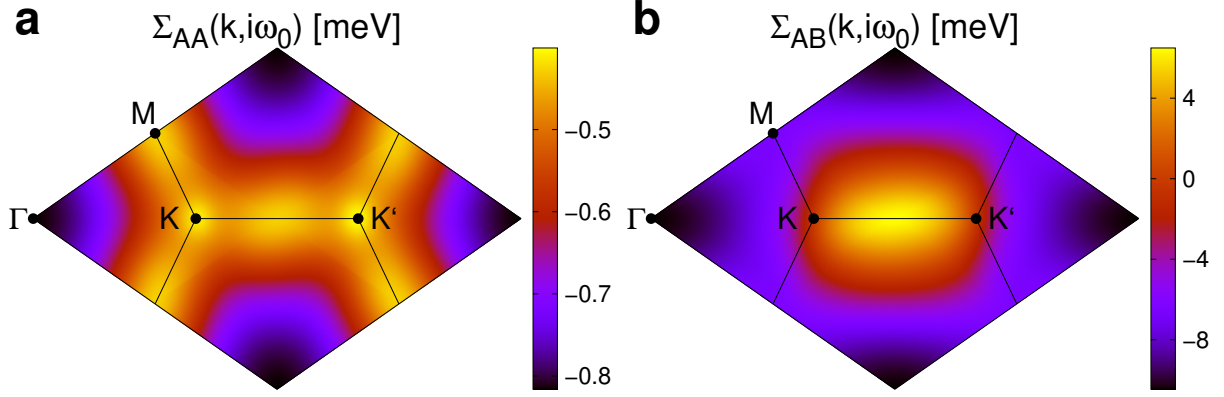
Supplementary Figure 4. **Momentum dependent intra- and inter-sublattice parts of the self-energy as obtained from the TPSC calculations**. The **a,** intra- and **b,** inter-sublattice parts of the self-energy are obtained at $T = 0.005$ eV = 58 K. The antiferromagnetic fluctuations lead to a significant non-local inter-sublattice self-energy Σ_{AB}

.

this exotic first-order transition in experiments by varying E_z.

E. DMFT and TPSC

As shown in the main text (Fig. 2), TPSC and DMFT consistently yield quasiparticle weights $Z \approx 0.75$ for temperatures in the range 60-230 K for non-twisted CCDW 1T-TaSe$_2$ bilayer. Also double occupancies $\langle n_\downarrow n_\uparrow \rangle \approx 0.15$ agree well between TPSC and DMFT in this temperature range. These results consistently put non-twisted CCDW 1T-TaSe$_2$ bilayer at intermediate local correlation strength and clearly far away from a paramagnetic Mott Hubbard transition.

The onset of non-local correlations can be inferred from the temperature dependent enhancement of antiferromagnetic susceptibilities and correlation lengths, which we obtained with TPSC and show in the main text (Fig. 2). These correlations manifest in sublattice off-diagonal contributions to the self-energy shown in Supplementary Figure 4.

[1] Mostofi, A. A. et al. wannier90: A tool for obtaining maximally-localised Wannier functions. *Computer Physics Communications* **178**, 685 – 699 (2008).

[2] Yu, P. Y. & Cardona, M. *Fundamentals of Semiconductors*, (Springer-Verlag Berlin Heidelberg, 2005).

[3] Dresselhaus, M. D., Dresselhaus, G. & Jorio, A. *Group Theory - Application to the Physics of Condensed Matter*, (Springer-Verlag Berlin Heidelberg, 2008).

[4] Slonczewski, J. C. & Weiss, P. R. Band structure of graphite. *Phys. Rev.* **109**, 272–279 (1958).

[5] Kochan, D., Irmer, S. & Fabian, J. Model spin-orbit Hamiltonians for graphene systems. *Phys. Rev. B* **95**, 165415 (2017).

[6] Gmitra, M., Kochan, D. & Fabian, J. Spin-orbit coupling in hydrogenated graphene. *Phys. Rev. Lett.* **110**, 246602 (2013).

[7] Kane, C. L. & Mele, E. J. Z_2 topological order and the Quantum Spin Hall effect. *Phys. Rev. Lett.* **95**, 146802 (2005).

[8] Soluyanov, A. A. & Vanderbilt, D. Computing topological invariants without inversion symmetry. *Phys. Rev. B* **83**, 235401 (2011).

[9] Amaricci, A., Budich, J., Capone, M., Trauzettel, B. & Sangiovanni, G. First-order character and observable signatures of topological quantum phase transitions. *Phys. Rev. Lett.* **114**, 185701 (2015).